Supplementary Information

Ecologically safe microplastic removal from saline water via temperature and buoyancy separation

Mehdi V. Bozorg[1] and Juan F. Torres[*1]

[1]ANU HEAT Lab, School of Engineering, The Australian National University, Canberra, Australia
[*]E-mail: felipe.torres@anu.edu.au

Supplementary Figures

Fig. 1 Size distribution of one-day-old *Artemia* nauplii . . . 2
Fig. 2 Temperature-dependent thermophysical properties of $3.4\,\mathrm{wt}\%$ saline for $\Delta T_{\mathrm{wall}} = 30\,\mathrm{K}$ . . . 3
Fig. 3 CFD results of vertical velocity of particles . . . 4
Fig. 4 Particle image velocimetry in the bio-friendly microplastic separator . . . 5
Fig. 5 Scalability of the multistage separation method . . . 6
Fig. 6 Effects of *Artemia* population density and temperature differential on thermotactic migration . . . 6
Fig. 7 Effect of surfactant on hydrophilicity of polyethylene and survival of one-day-old *Artemia* . . . 7
Fig. 8 Temperatures of the upper and lower walls during the multi-stage separation process . . . 8
Fig. 9 Experimental setup to assess the proposed bio-friendly separation method . . . 9
Fig. 10 Simple theoretical framework of microplastic transport and channel design principles . . . 10
Fig. 11 Mesh and time-step independence of the computational fluid dynamics simulations . . . 11
Fig. 12 Trajectory of a spherical microplastic particle in an isothermal separation channel . . . 12

Supplementary Tables

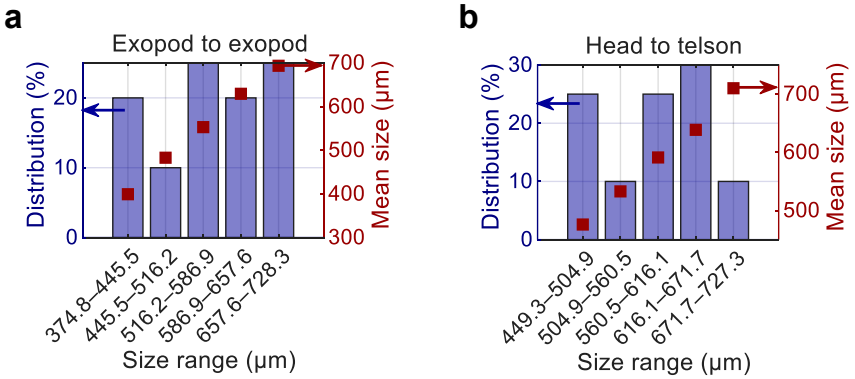
Table 1 Raw measurements and separation efficiencies of the two-stage separation process . . . 13
Table 2 Raw measurements and separation efficiencies of the three-stage separation process . . . 13
Table 3 Flow conditions and Reynolds numbers for different inlet flow rates . . . 13
Table 4 Hydrodynamic parameters for light microplastics . . . 14
Table 5 Hydrodynamic parameters for heavy microplastics . . . 14

Supplementary Videos (captions)

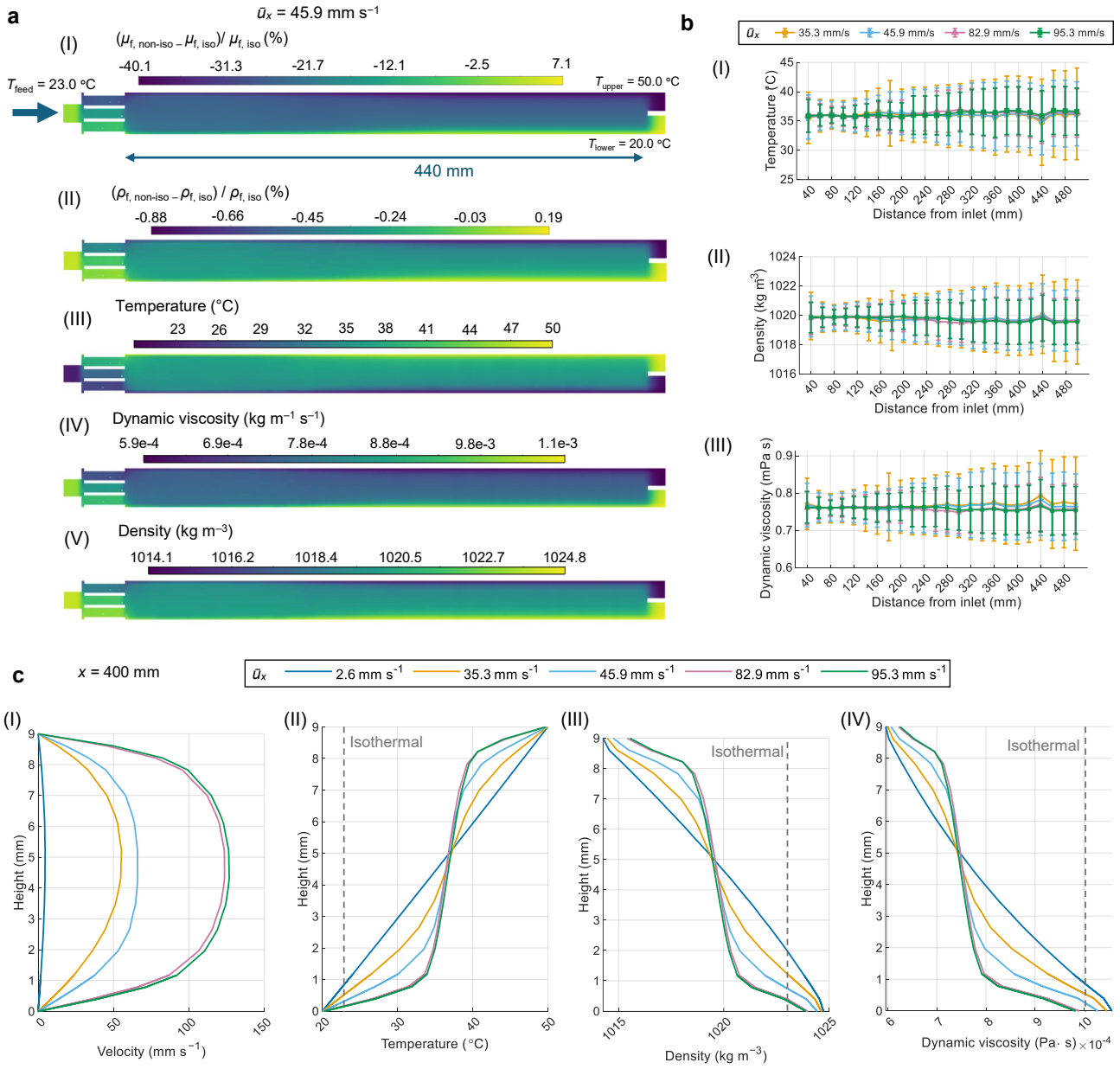
Video 1 Transport of one-day-old *Artemia* nauplii at moderate flow velocities in the separation channel . . . 15
Video 2 Visualisation of flow patterns and species transport within the laser sheet for single-component saline mixtures . . . 15
Video 3 Thermotactic migration of one-day-old *Artemia* nauplii under a subtle flow and moderate temperature differentials . . . 15

Supplementary Methods

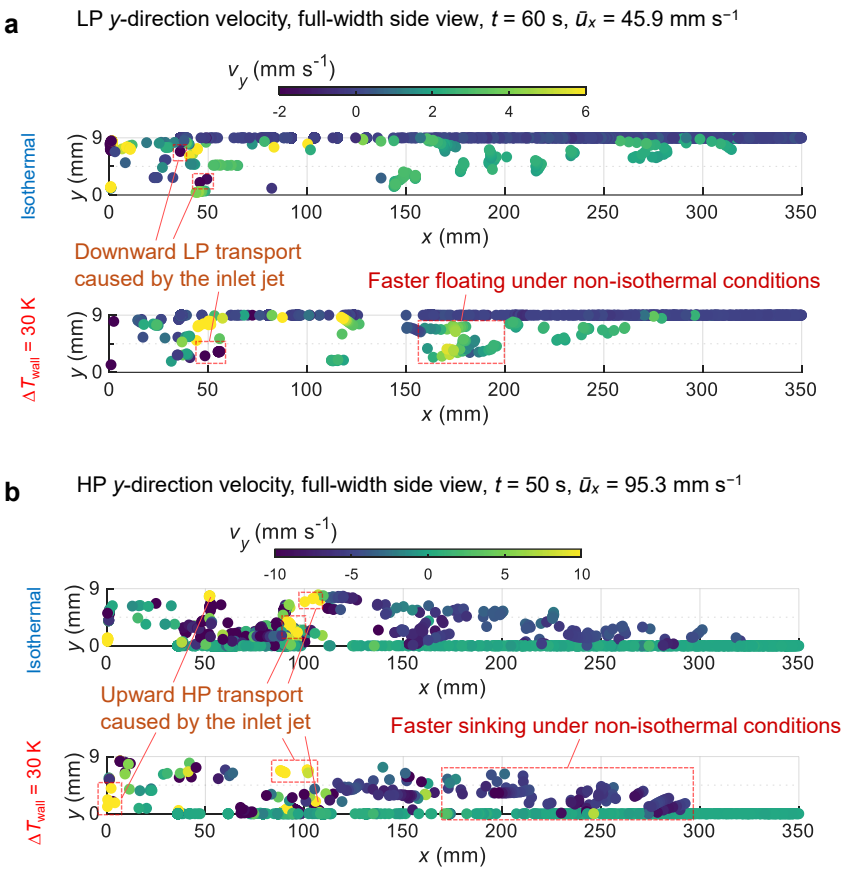
Method 1 Hydrodynamics of microplastic transport . . . 16



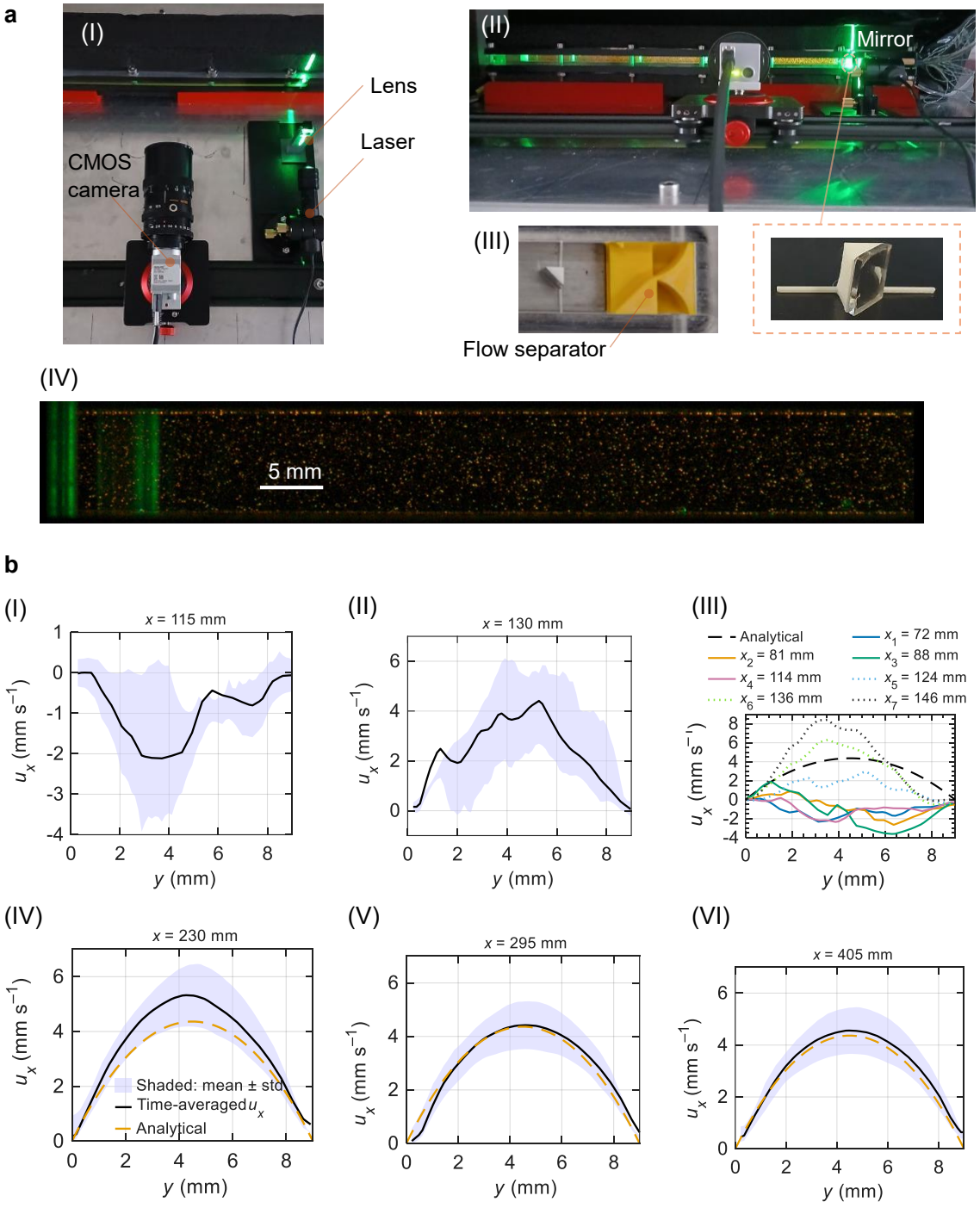
Supplementary Fig. 1 | Size distribution of one-day-old *Artemia* nauplii. a, Taking the distance from exopod to exopod as the size metric, as shown in Fig. 1bI. **b**, Taking head to telson as the size metric. Figure 1cI reports the equivalent diameter d_{eq}.



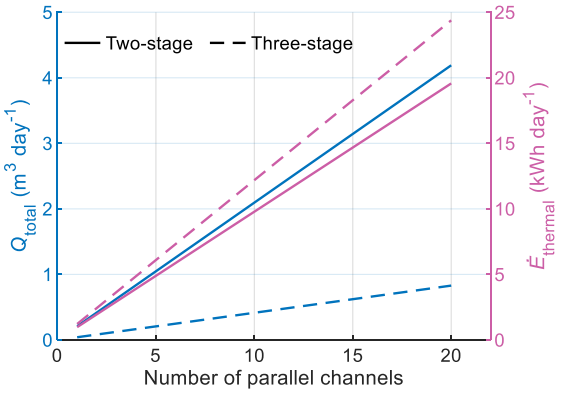
Supplementary Fig. 2 | Temperature-dependent thermophysical properties of $3.4\,\mathrm{wt\%}$ saline for $\Delta T_{\mathrm{wall}} = 30\,\mathrm{K}$. On the mid-vertical plane along the rectangular channel. **a**, Contours of (I) relative change in the dynamic viscosity of saline water, $(\mu_{\mathrm{f,heated}} - \mu_{\mathrm{f,iso}})/\mu_{\mathrm{f,iso}} \times 100\%$, between the isothermal case at $23\,^{\circ}\mathrm{C}$ and the non-isothermal case at $\Delta T_{\mathrm{wall}} = 30\,\mathrm{K}$. (II) Corresponding relative change in the density of saline water, $(\rho_{\mathrm{f,heated}} - \rho_{\mathrm{f,iso}})/\rho_{\mathrm{f,iso}} \times 100\%$. The fields of fluid (III) temperature, (IV) dynamic viscosity, and (V) density are shown for an average fluid velocity of $45.9\,\mathrm{mm\,s^{-1}}$. **b**, At different distances from the inlet, time- and height-averaged temperature, density, and dynamic viscosity for different values of average fluid velocities $\bar{u}_x$ indicted in the legend. **c**, At $x = 400\,\mathrm{mm}$, streamwise velocity u_x, temperature T, density ρ, and dynamic viscosity μ profiles across the channel height y for the wide range of average fluid velocities indicted in the legend. The isothermal case is indicated in (II–IV) to better understand the regions where changes in thermophysical properties due to ΔT_{wall} may affect MP transport.



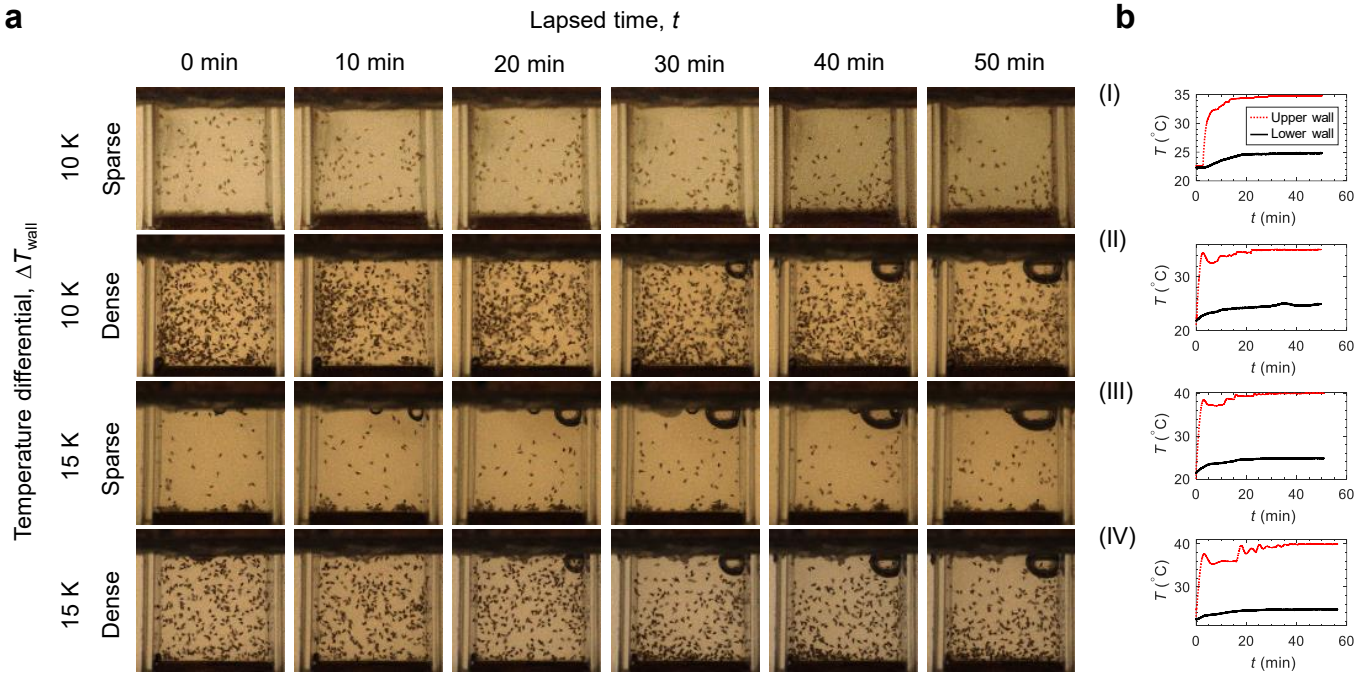
Supplementary Fig. 3 | CFD results of vertical velocity of particles. The temperature was maintained at $23.0\,^{\circ}\mathrm{C}$ under isothermal condition, while the lower and upper walls were maintained at $20\,^{\circ}\mathrm{C}$ and $50\,^{\circ}\mathrm{C}$, respectively, under non-isothermal or heated condition. **a**, Side view of the full-width ($z = 0$ to $z = 27\,\mathrm{mm}$) of LP distributions coloured by particle y-direction velocity at $t = 60\,\mathrm{s}$ for a mean velocity of $\bar{u}_x = 45.9\,\mathrm{mm\,s^{-1}}$ under $23.0\,^{\circ}\mathrm{C}$ isothermal and $\Delta T_{\mathrm{wall}} = 30\,\mathrm{K}$ heated conditions. **b**, Same as the previous panel but for $t = 50\,\mathrm{s}$ and $\bar{u}_x = 95.3\,\mathrm{mm\,s^{-1}}$.



Supplementary Fig. 4 | Particle image velocimetry in the bio-friendly microplastic separator. a, Experimental configuration for particle image velocimetry (PIV) in the rectangular channel used for bio-friendly separation. (I) Top-view photo of the setup, (II) side-view photo; the inset shows a flat mirror placed inside the channel to deviate the laser sheet placing it on the mid-vertical plane of the channel, (III) top view near the outlet with the mirror and flow separator, and (IV) representative raw PIV image showing a snapshot of the tracer location. $50\,\mu\mathrm{m}$ tracer particles, which were used as MP samples, were visualised on the vertical mid-plane of the channel, as indicated in the schematic of Fig. 5a. **b**, Measured velocity profiles, $u_x\,(y)$, on mid-plane for an average velocity of $\bar{u} = 2.6\,\mathrm{mm\,s^{-1}}$, obtained using tracers with density of $995\,\mathrm{kg\,m^{-3}}$, suspended in deionised water under isothermal conditions of $22.6\,^{\circ}\mathrm{C}$. $u_x\,(y)$ at different streamwise positions from the inlet: (I) $x = 115\,\mathrm{mm}$, (II) $x = 130\,\mathrm{mm}$, (III) seven different positions near the inlet, showing how the flow gradually approaches the analytical solution presented in Supplementary Method 1.3, (IV) $x = 230\,\mathrm{mm}$, (V) $x = 295\,\mathrm{mm}$, and (VI) $x = 405\,\mathrm{mm}$. Supplementary Video 2a shows the recorded videos on which PIV is based on.

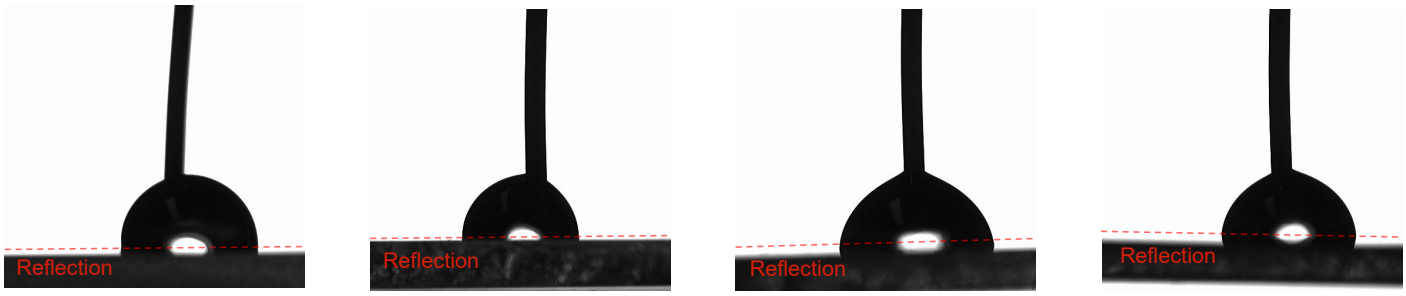


Supplementary Fig. 5 | Scalability of the multistage separation method. MP remediation capacity and energy consumption are obtained for three- and two-stage separation processes with $\bar{u}_2 = 23.1\,\mathrm{mm\,s^{-1}}$ for multiple parallel separation channels. Noting that the separation efficiencies for multiple parallel channels are the same as those for a single channel, i.e., the overall separation efficiencies for the three- and two-stage processes are $63.8\% \pm 10.1\%$ and $42.2\% \pm 5.3\%$, respectively. Using a wider single channel instead of multiple channels with the same overall width could decrease energy consumption by reducing sidewall effects on the internal temperature and velocity profiles.



Supplementary Fig. 6 | Effects of *Artemia* population density and temperature differential on thermotactic migration. The temperature of the lower wall was fixed at 25.0 °C. For cases with $\Delta T_{\mathrm{wall}} = 10\,\mathrm{K}$, the upper wall temperature was set to 35.0 °C, whereas for cases with $\Delta T_{\mathrm{wall}} = 15\,\mathrm{K}$, it was set to 40.0 °C. **a**, Observed *Artemia* distribution at different times for $\Delta T_{\mathrm{wall}} = 10\,\mathrm{K}$ and 15 K under sparse and dense *Artemia* populations. **b**, Temperature histories for the experiments: (I) sparse population at $\Delta T_{\mathrm{wall}} = 10\,\mathrm{K}$, (II) dense population at $\Delta T_{\mathrm{wall}} = 10\,\mathrm{K}$, (III) sparse population at $\Delta T_{\mathrm{wall}} = 15\,\mathrm{K}$, and (IV) dense population at $\Delta T_{\mathrm{wall}} = 15\,\mathrm{K}$.

a



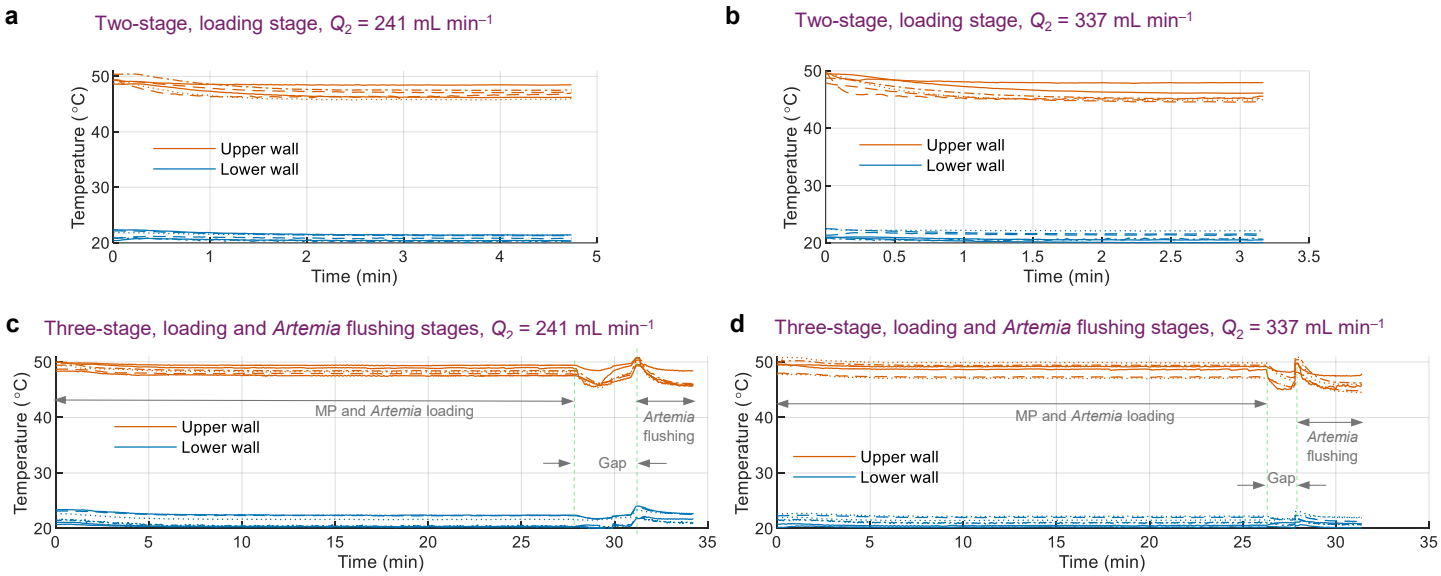
DI water | DI water-20 mg L^{-1} CAPB | DI water-50 mg L^{-1} CAPB | DI water-100 mg L^{-1} CAPB

b

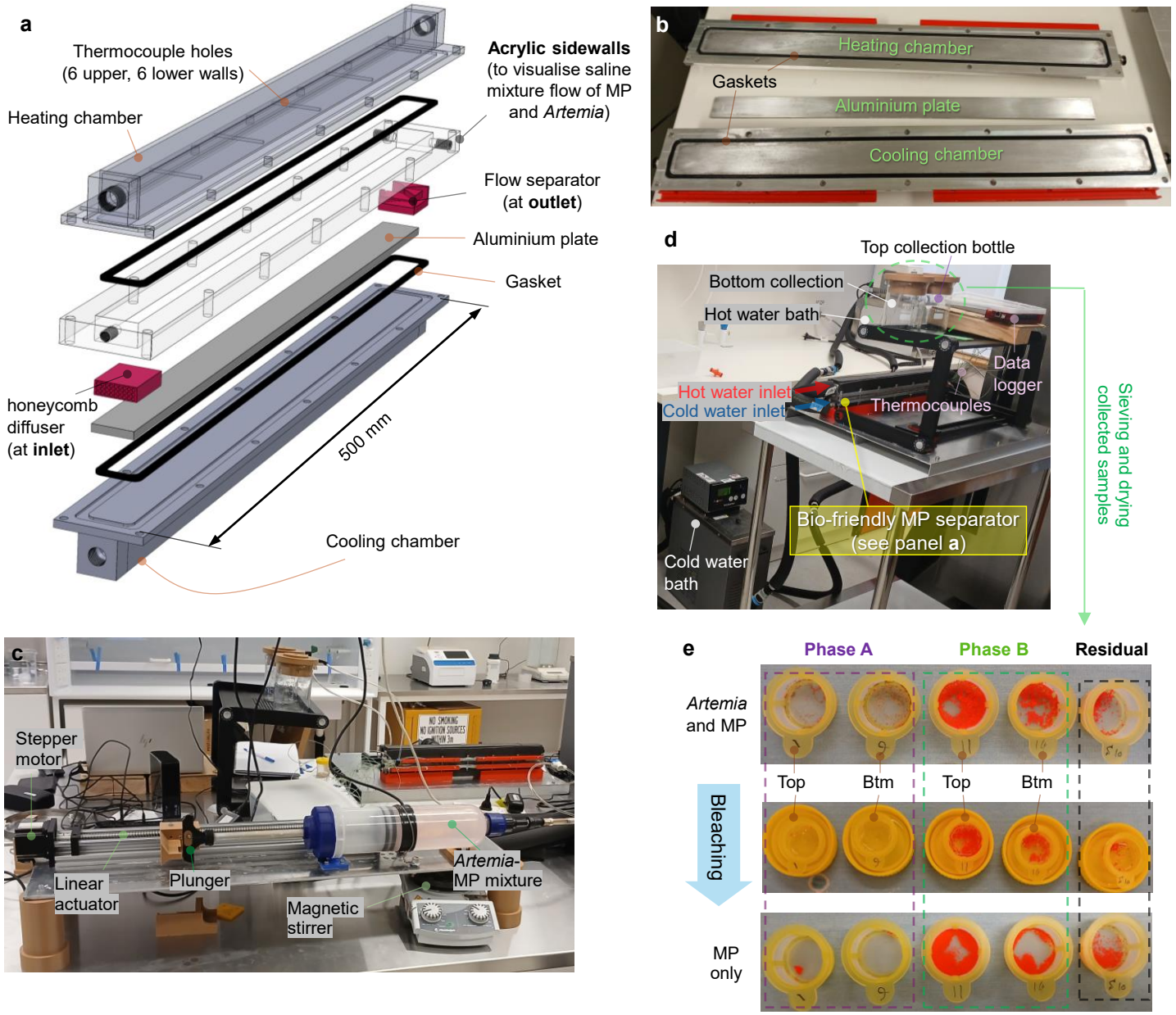
Assessment of biosurfactant toxicity toward *Artemia*

Surfactant	Abbreviation	Concentration (mg L^{-1})	Solution volume (mL)	Survival
Lecithin (Soybean phospholipid)	LLEC	300	50	No
Sodium Lauryl Ether Sulphate	SLES	300	50	No
Decyl Glucoside	DG	300	50	No
Coco Amido Propyl Betaine	CAPB	300	50	Yes, >24 hrs

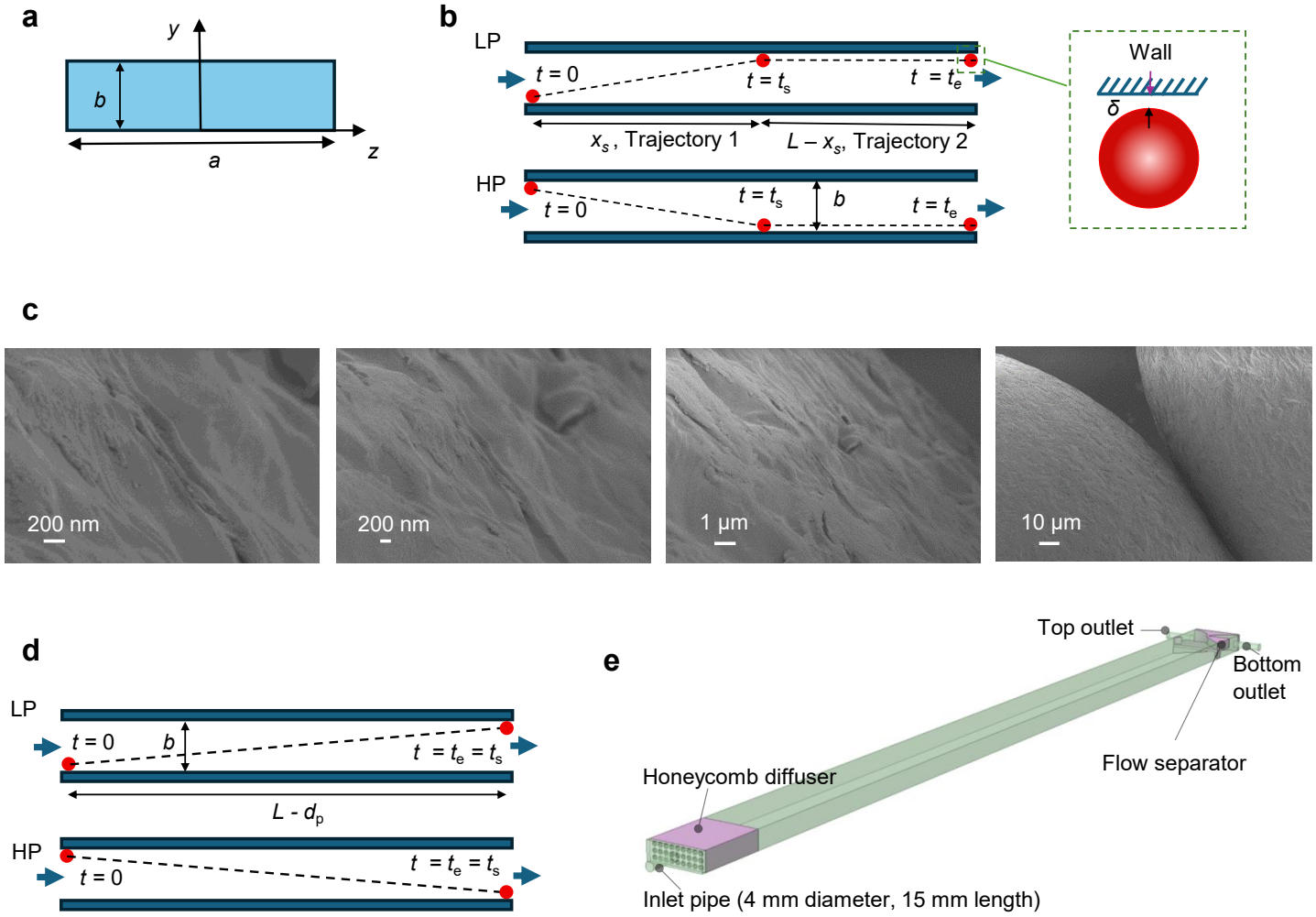
Supplementary Fig. 7 | Effect of surfactant on hydrophilicity of polyethylene and survival of one-day-old *Artemia*. **a**, Effect of the concentration of cocamidopropyl betaine (CAPB), a surfactant derived from coconut oil and dimethylaminopropylamine, on the hydrophilicity of polyethylene, which is the MP material. The images show variation in the contact angle of a droplet of CAPB–DI water solution on a polyethylene sheet. For CAPB concentrations of $0\,\mathrm{mg\,L^{-1}}$ (DI water only), $20\,\mathrm{mg\,L^{-1}}$, $50\,\mathrm{mg\,L^{-1}}$, and $100\,\mathrm{mg\,L^{-1}}$, the measured contact angles were $94.8° \pm 1.4°$, $87.7° \pm 0.7°$, $79.9° \pm 1.3°$, and $80.6° \pm 0.9°$, respectively. The progressive decrease in contact angle with increasing CAPB concentration from $0\,\mathrm{mg\,L^{-1}}$ to $50\,\mathrm{mg\,L^{-1}}$ indicates enhanced wettability of the polyethylene surface by the CAPB-containing DI water solutions. Increasing the CAPB concentration from $50\,\mathrm{mg\,L^{-1}}$ to $100\,\mathrm{mg\,L^{-1}}$ had no significant effect on wettability of polyethylene. However, based on our observations of hydrophilicity behaviour of spherical polyethylene particles in $3.4\,\mathrm{wt\%}$ saline, with a nominal diameter of $390\,\mu\mathrm{m}$, a CAPB concentration of $200\,\mathrm{mg\,L^{-1}}$ was selected for the experiments. **b**, The results of toxicity tests of four types of potential bio-surfactants on the survival of *Artemia* at surfactant concentration of $300\,\mathrm{mg\,L^{-1}}$. CAPB was found to be bio-friendly given the near-complete survival of *Artemia* nauplii after more than $24\,\mathrm{h}$. The experiments in the bio-friendly separation flow were conducted with CAPB concentration at $200\,\mathrm{mg\,L^{-1}}$.



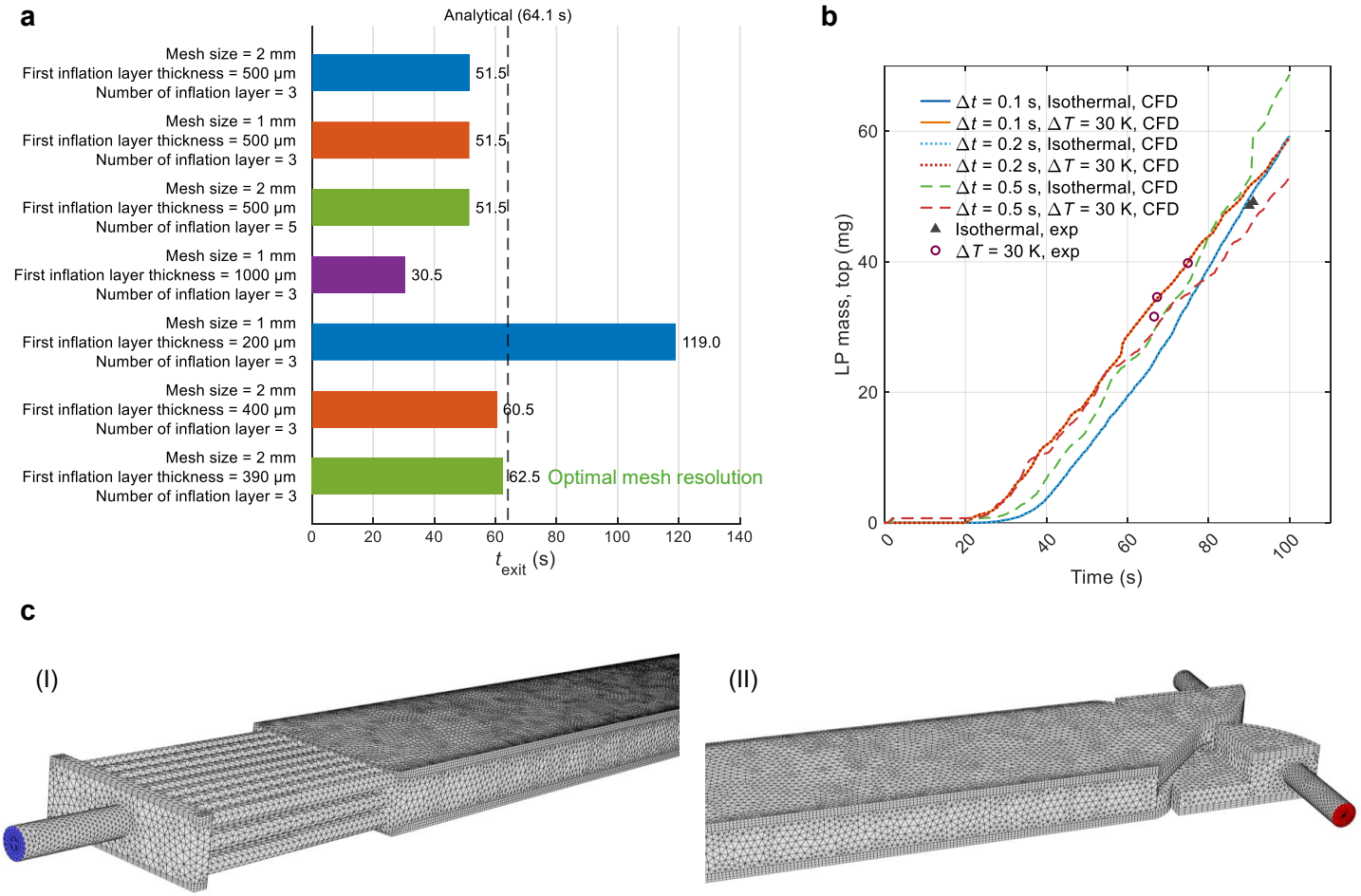
Supplementary Fig. 8 | Temperatures of the upper and lower walls during the multi-stage separation process. a, During the two-stage separation process, wall temperatures of the loading-stage (MP and *Artemia* nauplii saline mixture) at a flow rate of $Q_2 = 241\,\mathrm{mL\,min^{-1}}$ ($\bar{u}_2 = 16.5\,\mathrm{mm\,s^{-1}}$). **b**, Subsequent wall temperatures of the loading-stage (MP and *Artemia* nauplii saline mixture) at a flow rate of $Q_2 = 337\,\mathrm{mL\,min^{-1}}$ ($\bar{u}_2 = 23.1\,\mathrm{mm\,s^{-1}}$). **c**, During the three-stage separation process, wall temperatures of the loading-stage (MP and *Artemia* nauplii saline mixture) at a flow rate of $Q_1 = 38\,\mathrm{mL\,min^{-1}}$ ($\bar{u}_2 = 2.6\,\mathrm{mm\,s^{-1}}$) and *Artemia* flushing stage at a flow rate of $Q_2 = 241\,\mathrm{mL\,min^{-1}}$ ($\bar{u}_2 = 16.5\,\mathrm{mm\,s^{-1}}$). **d**, Subsequent wall temperatures of the loading-stage (MP and *Artemia* nauplii saline mixture) at a flow rate of $Q_1 = 38\,\mathrm{mL\,min^{-1}}$ ($\bar{u}_2 = 2.6\,\mathrm{mm\,s^{-1}}$) and *Artemia* flushing stage at a flow rate of $Q_2 = 337\,\mathrm{mL\,min^{-1}}$ ($\bar{u}_2 = 23.1\,\mathrm{mm\,s^{-1}}$).



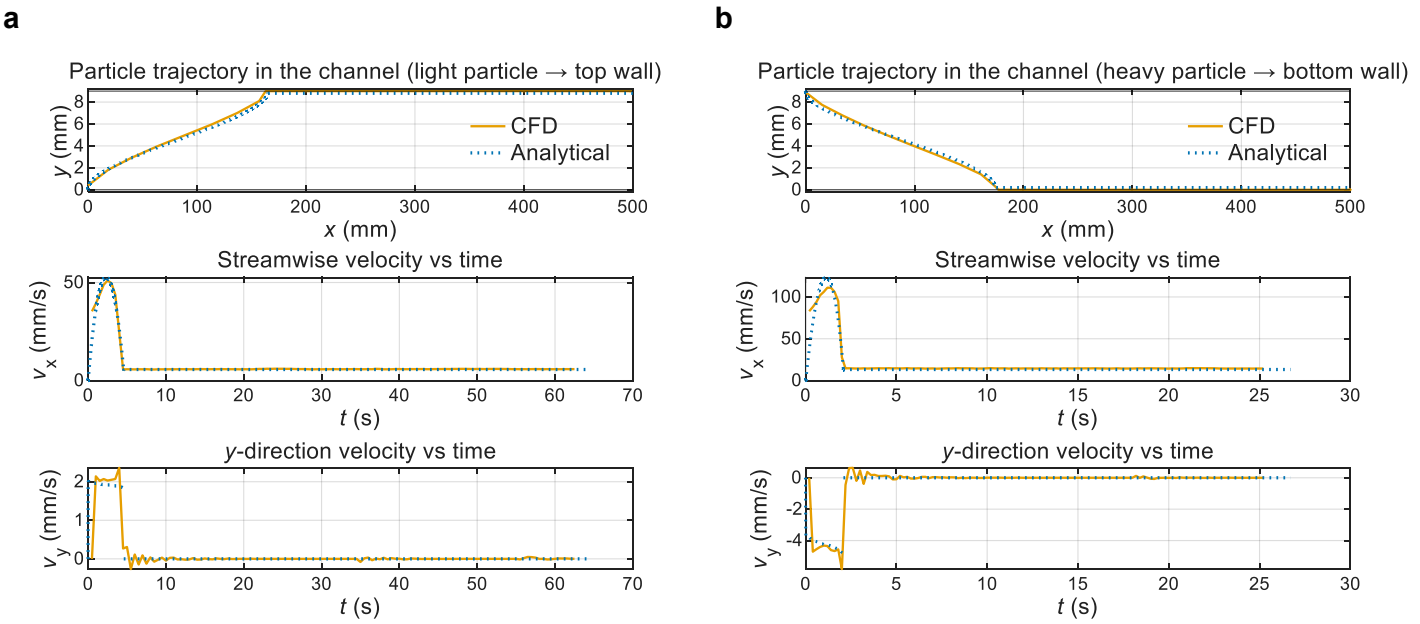
Supplementary Fig. 9 | Experimental setup to assess the proposed bio-friendly separation method. a, Exploded view of the computer-aided design (CAD) model of the rectangular duct with heating and cooling chambers. The temperature differential normal to the flow can be inverted by simply swapping the hot and cold water streams in the chambers, as it was done once in Fig. 3 to check the mixing effect due to the thermally unstable configuration. **b**, Photo showing the top view of the disassembled cooling and heating chambers. Note that gaskets are introduced to avoid leakage. **c**, Photo of the pumping setup, which includes the large syringe pump and a magnetic stirrer that keeps the feed mixture as homogeneous as possible. Without stirring, *Artemia* nauplii and heavy MP sink, while light MP float. **d**, Photo that captures the entire experimental setup, including the cooling and heating water baths, from which the cold and hot water enter the bio-friendly MP separator, and temperature-monitoring setups. **e**, Collected samples in the multi-stage process for determining the masses of dried MPs and *Artemia* nauplii. A process of bleaching, rinsing and drying is used to discern between the mass of MPs and *Artemia* nauplii.



Supplementary Fig. 10 | Simple theoretical framework of microplastic transport and channel design principles. a, Coordinates and geometric dimensions of the rectangular duct cross-section used for the analytical velocity profile correlation. **b**, Schematics of two-trajectory transport model of light and heavy microplastics (LP and HP, respectively) in a rectangular channel. **c**, Scanning electron microscopy (SEM) images of spherical polyethylene microplastics (MPs) with a nominal diameter of 390 µm. **d**, Schematics of the limiting inlet velocity for LP and HP in a rectangular channel of length L. Velocities exceeding this threshold prevent sufficient particle migration along the entire height of the channel, reducing the feasibility of MP–microorganism separation. **e**, Model of the separation channel showing the inlet pipe, honeycomb diffuser, and flow splitter. These components are omitted in the analytical model and simplified computational fluid dynamics (CFD) simulations of single-particle transport, while they are included in CFD simulations to reproduce the experimental configuration (Section 2.2).



Supplementary Fig. 11 | Mesh and time-step independence of the computational fluid dynamics simulations. a, Mesh independence analysis for a single LP particle with a diameter of $390\,\mu\mathrm{m}$ transported through a rectangular duct, without considering the inlet pipe, honeycomb diffuser, or flow splitter. Simulations were performed under isothermal conditions at $23.0\,^{\circ}\mathrm{C}$ with an average fluid velocity of $\bar{u} = 35.3\,\mathrm{mm\,s^{-1}}$. t_{exit} denotes the time required for the particle to exit the duct. CFD predictions obtained using different mesh resolutions were compared with the analytical result described in Supplementary Method 1.3. **b**, Time-step independence analysis for the transport of a single LP particle with a diameter of $390\,\mu\mathrm{m}$ through the separation duct, including the inlet pipe, honeycomb diffuser, and flow splitter, under isothermal and non-isothermal conditions ($\Delta T_{\mathrm{wall}} = 30\,\mathrm{K}$). The average mixture velocity within the duct was $\bar{u} = 45.9\,\mathrm{mm\,s^{-1}}$. The simulation results are compared with the experimental data. **c**, The computational mesh used in the CFD simulations: (I) near the inlet pipe and honeycomb diffuser and (II) near the outlets. The hybrid mesh consists of a structured mesh near the upper and lower walls and an unstructured mesh elsewhere. The structured mesh improves the accuracy of the laminar boundary layer calculation, while the unstructured mesh handles the irregular flow in the inlet pipe, honeycomb diffuser, flow splitter, and channel centre more robustly.



Supplementary Fig. 12 | Trajectory of a spherical microplastic particle in an isothermal separation channel. These modelling results show the trajectory, time required for the particles to float or sink, and the corresponding settling distance measured from the inlet, for different mean flow velocities ($\bar{u}$). The spherical MP has diameter of $390\,\mu\mathrm{m}$ and the flow is isothermal at $23.0\,^{\circ}\mathrm{C}$. The effects of the $4\,\mathrm{mm}$ diameter inlet pipe and honeycomb diffuser are neglected, while the rectangular cross-section of the channel is used as the inlet. **a**, A single light MP, or LP, released from the lower wall central point of the channel with an average flow velocity of $\bar{u} = 35.3\,\mathrm{mm\,s^{-1}}$. **b**, A single heavy MP, or HP, released from the upper wall central point of the channel when $\bar{u} = 82.9\,\mathrm{mm\,s^{-1}}$. Particle trajectories and streamwise (x direction) and transverse (y direction) velocities are compared between the analytical solutions of the ordinary differential equations (ODEs) for particle momentum and the CFD results.

Supplementary Table 1 | Raw measurements and separation efficiencies of the two-stage separation process. The table lists the collected and residual masses in Phases A and B, and the corresponding separation performance metrics in a two-stage separation process. The microorganism and MP loading flow rate is $Q_2 = 241\,\mathrm{mL\,min^{-1}}$ or $337\,\mathrm{mL\,min^{-1}}$ (Stage 1), and the MP flushing flow rate is $Q_3 = 1208\,\mathrm{mL\,min^{-1}}$ (Stage 2). In the subscripts, A is Phase A (Stage 1), B is Phase B (Stage 2), t is the top outlet, b is the bottom outlet, P denotes microplastic material, O microorganism, and R residual. Q is flow rate, M is mass, *SR* is separation ratio, and η is separation efficiency.

Q_2 ($\mathrm{mL\,min^{-1}}$)	$M_{\mathrm{P,t,A}}$ (mg)	$M_{\mathrm{P,b,A}}$ (mg)	$M_{\mathrm{O,t,A}}$ (mg)	$M_{\mathrm{O,b,A}}$ (mg)	$M_{\mathrm{P,t,B}}$ (mg)	$M_{\mathrm{P,b,B}}$ (mg)	$M_{\mathrm{O,t,B}}$ (mg)	$M_{\mathrm{O,b,B}}$ (mg)	$M_{\mathrm{P,R}}$ (mg)	$M_{\mathrm{O,R}}$ (mg)	$SR_{\mathrm{O,A}}$ (%)	$SR_{\mathrm{P,A}}$ (%)	η_{O} (%)	η_{P} (%)	η (%)
241	0.9	0.4	0.7	9.1	115.5	49.0	0.7	9.8	46.9	0.8	85.7 ± 1.9	35.8 ± 11.7	43.1 ± 0.7	77.8 ± 0.1	33.5 ± 0.5
241	1.2	0.3	6.7	27.9	98.7	49.8	3.3	31.7	39.5	1.0	61.3 ± 0.5	60.0 ± 11.0	39.5 ± 0.2	79.0 ± 0.1	31.2 ± 0.2
241	1.0	0.5	2.7	8.8	99.6	57.8	0.5	3.2	35.8	0.0	53.0 ± 1.3	33.3 ± 9.9	57.9 ± 1.1	81.4 ± 0.1	47.1 ± 0.9
241	1.0	0.8	3.2	5.0	112.8	62.8	1.2	1.3	30.3	0.3	22.0 ± 1.8	11.1 ± 7.9	45.5 ± 1.3	85.0 ± 0.1	38.6 ± 1.1
241	1.2	0.2	1.2	4.9	94.0	51.1	0.9	2.7	28.4	0.4	60.7 ± 2.7	71.4 ± 12.4	48.5 ± 1.5	83.6 ± 0.1	40.6 ± 1.2
337	4.4	1.2	4.2	10.9	110.5	58.3	0.3	2.7	40.8	0.1	44.4 ± 1.0	57.1 ± 2.9	59.9 ± 0.9	80.5 ± 0.1	48.2 ± 0.7
337	5.8	1.0	2.2	5.0	120.1	69.3	0.3	0.8	56.2	0.0	38.9 ± 2.1	70.6 ± 2.5	60.2 ± 2.0	77.3 ± 0.1	46.6 ± 1.6
337	5.4	1.2	3.8	10.1	115.9	72.9	1.3	3.9	41.7	0.4	45.3 ± 1.1	62.5 ± 2.5	51.6 ± 0.8	81.9 ± 0.1	42.3 ± 0.6
337	6.5	1.2	1.6	4.1	115.8	89.2	1.2	1.7	32.5	0.8	43.9 ± 2.7	68.8 ± 2.2	43.6 ± 1.5	86.3 ± 0.1	37.6 ± 1.3
337	3.6	1.1	1.5	5.0	113.6	78.1	1.1	3.1	37.2	0.8	53.8 ± 2.5	53.2 ± 3.4	43.5 ± 1.2	83.6 ± 0.1	36.4 ± 1.0

Supplementary Table 2 | Raw measurements and separation efficiencies of the three-stage separation process. The table shows the collected and residual masses in Phases A and B, and the corresponding separation performance metrics in a three-stage separation process. The flow rate of microorganism and MP loading is $Q_1 = 38\,\mathrm{mL\,min^{-1}}$ (Stage 1), MO flushing flow rate is $Q_2 = 241$ or $337\,\mathrm{mL\,min^{-1}}$ (Stage 2), and MP flushing flow rate is Q_3=$1208\,\mathrm{mL\,min^{-1}}$ (Stage 3). The caption of Supplementary Table 1 denotes the subscript definitions.

Q_2 ($\mathrm{mL\,min^{-1}}$)	$M_{\mathrm{P,t,A}}$ (mg)	$M_{\mathrm{P,b,A}}$ (mg)	$M_{\mathrm{O,t,A}}$ (mg)	$M_{\mathrm{O,b,A}}$ (mg)	$M_{\mathrm{P,t,B}}$ (mg)	$M_{\mathrm{P,b,B}}$ (mg)	$M_{\mathrm{O,t,B}}$ (mg)	$M_{\mathrm{O,b,B}}$ (mg)	$M_{\mathrm{P,R}}$ (mg)	$M_{\mathrm{O,R}}$ (mg)	$SR_{\mathrm{O,A}}$ (%)	$SR_{\mathrm{P,A}}$ (%)	η_{O} (%)	η_{P} (%)	η (%)
241	19.5	1.6	0.5	13.3	141.4	69.0	0.2	9.8	9.6	0.8	92.8 ± 1.4	84.8 ± 0.9	54.1 ± 0.6	95.4 ± 0.1	51.6 ± 0.6
241	14.6	2.0	0.3	14.4	137.9	80.2	1.5	14.4	13.3	2.6	95.9 ± 1.3	75.9 ± 1.1	43.4 ± 0.4	93.8 ± 0.1	40.7 ± 0.4
241	8.7	0.8	1.2	6.9	143.1	118.5	2.1	2.4	12.3	1.1	70.4 ± 2.1	83.2 ± 1.9	50.4 ± 1.1	95.4 ± 0.1	48.0 ± 1.1
241	17.4	0.9	1.0	10.6	127.3	112.5	1.9	6.8	36.7	1.8	82.8 ± 1.6	90.2 ± 1.0	48.0 ± 0.7	87.2 ± 0.1	41.8 ± 0.6
241	26.7	3.2	1.4	18.1	116.1	114.2	0.1	12.0	21.9	1.0	85.9 ± 1.0	78.4 ± 0.6	55.7 ± 0.5	91.1 ± 0.1	50.7 ± 0.4
241	34.4	1.5	1.5	17.4	112.5	97.0	0.8	9.4	24.3	0.2	84.1 ± 1.0	91.6 ± 0.5	59.4 ± 0.6	90.4 ± 0.1	53.7 ± 0.5
241	8.0	1.6	0.3	4.9	111.6	94.5	0.7	0.2	37.5	0.4	88.5 ± 3.6	66.7 ± 1.8	75.4 ± 3.0	84.6 ± 0.1	63.7 ± 2.6
241	9.4	2.6	0.3	4.4	132.4	81.2	0.5	1.7	19.4	0.4	87.2 ± 4.0	56.7 ± 1.4	60.3 ± 2.3	91.0 ± 0.1	54.9 ± 2.1
337	8.2	1.6	1.4	9.1	86.6	74.9	0.0	1.3	15.1	0.8	73.3 ± 1.7	67.3 ± 1.7	72.2 ± 1.5	91.0 ± 0.1	65.7 ± 1.4
337	6.9	1.6	1.1	20.2	92.6	62.5	1.0	12.0	13.5	1.7	89.7 ± 0.9	62.4 ± 2.0	56.1 ± 0.4	91.5 ± 0.2	51.3 ± 0.4
337	48.5	2.0	1.6	7.4	106.4	81.7	0.0	1.5	32.7	0.2	64.4 ± 1.9	92.1 ± 0.4	69.2 ± 1.7	87.2 ± 0.1	60.3 ± 1.5
337	58.4	3.4	1.5	10.4	116.1	99.3	0.6	2.8	14.4	0.0	74.8 ± 1.5	89.0 ± 0.3	68.0 ± 1.2	93.9 ± 0.1	63.8 ± 1.1
337	19.6	9.0	5.9	20.4	102.6	117.5	0.6	2.8	18.5	0.6	55.1 ± 0.6	37.1 ± 0.5	67.3 ± 0.6	89.7 ± 0.1	60.4 ± 0.5
337	41.6	2.0	1.2	7.4	104.9	115.7	0.4	2.9	29.0	0.6	72.1 ± 2.0	90.8 ± 0.4	59.2 ± 1.3	89.4 ± 0.1	52.9 ± 1.2
337	31.6	3.6	0.5	6.8	103.6	119.9	0.2	0.3	25.9	0.1	86.3 ± 2.6	79.5 ± 0.5	86.1 ± 2.7	89.6 ± 0.1	77.2 ± 2.5
337	30.1	5.7	0.2	8.2	105.7	124.7	0.0	0.6	21.3	0.4	95.2 ± 2.3	68.2 ± 0.5	87.2 ± 2.3	90.6 ± 0.1	79.0 ± 2.1

Supplementary Table 3 | Flow conditions and Reynolds numbers for different inlet flow rates. $\bar{u}_{\mathrm{pipe}}$ is the mean velocity in the $4\,\mathrm{mm}$ inlet pipe, $\bar{u}_{\mathrm{cha}}$ is the average velocity in the separation channel, L_e is the hydrodynamic entrance length, $\mathrm{Re}_{\mathrm{pipe}}$ is Reynolds number in the $4\,\mathrm{mm}$ inlet pipe and $\mathrm{Re}_{\mathrm{cha}}$ is Reynolds number in the channel.

Q ($\mathrm{mL\,min^{-1}}$)	$\bar{u}_{\mathrm{pipe}}$ ($\mathrm{m\,s^{-1}}$)	$\bar{u}_{\mathrm{cha}}$ ($\mathrm{m\,s^{-1}}$)	L_e (mm)	$\mathrm{Re}_{\mathrm{pipe}}$	$\mathrm{Re}_{\mathrm{cha}}$
241	0.3196	0.0165	142.7	1211.1	211.4
337	0.447	0.0231	199.5	1693.5	295.6
515	0.683	0.0353	304.9	2588.0	451.7
669	0.887	0.0459	396.1	3361.8	586.8
933	1.237	0.0640	552.3	4688.5	818.3
1021	1.354	0.0700	604.4	5130.7	895.5
1208	1.602	0.0829	715.2	6070.4	1059.5
1390	1.844	0.0953	822.9	6985.0	1219.1

Supplementary Table 4 | Hydrodynamic parameters for light microplastic. Q is the flow rate, $\mathrm{St}_{\mathrm{pipe}}$ and $\mathrm{St}_{\mathrm{cha}}$ are the Stokes numbers based on the inlet pipe and duct velocities, respectively, x_s is the settling distance calculated from analytical method, $x_{s,\mathrm{CFD}}$ is the settling distance obtained from CFD, t_s is the settling time, and t_{exit} and $t_{\mathrm{exit,CFD}}$ are the particle residence times obtained using analytical and CFD methods, respectively. The analytical results were obtained by solving the ODEs governing the momentum balance of a single particle. In both analytical and CFD methods, the particle was released from the lower-wall middle-point.

Q (mL min^{-1})	$\mathrm{St}_{\mathrm{pipe}}$	$\mathrm{St}_{\mathrm{cha}}$	x_s (mm)	x_s, CFD (mm)	t_s (s)	t_{exit} (s)	$t_{\mathrm{exit,CFD}}$ (s)
241	0.622	2.6×10^{-4}	77.3	75.6	4.6	165.1	164.5
337	0.870	3.6×10^{-4}	108.1	107.7	4.6	111.0	109.0
515	1.329	5.5×10^{-4}	165.2	164.0	4.6	64.1	62.0
669	1.7269	7.1×10^{-4}	214.6	209.3	4.6	43.6	42.0
933	2.4083	1.0×10^{-3}	299.3	291.1	4.6	24.3	23.4
1021	2.6355	1.1×10^{-3}	327.6	317.6	4.6	20.0	19.4
1208	3.1182	1.3×10^{-3}	387.7	372.2	4.6	13.1	13.0
1390	3.5880	1.5×10^{-3}	446.2	407.6	4.6	8.1	9.4

Supplementary Table 5 | Hydrodynamic parameters for heavy microplastic. Refer to Supplementary Table 4 for the nomenclature. In both the analytical analysis and CFD simulations, the initial release point was set at the upper-wall middle-point of the the inlet cross-section of the rectangular duct.

Q (mL min^{-1})	$\mathrm{St}_{\mathrm{pipe}}$	$\mathrm{St}_{\mathrm{cha}}$	x_s (mm)	$x_{s,\mathrm{CFD}}$ (mm)	t_s (s)	t_{exit} (s)	$t_{\mathrm{exit,CFD}}$ (s)
241	0.6815	2.8×10^{-4}	34.8	35.9	2.1	178.7	175.2
337	0.9529	3.9×10^{-4}	48.7	50.2	2.1	124.6	121.6
515	1.4563	6.0×10^{-4}	74.4	76.7	2.1	77.7	74.8
669	1.8920	7.8×10^{-4}	96.7	99.7	2.1	57.2	55.2
933	2.6380	1.1×10^{-3}	135.0	138.0	2.1	37.9	35.4
1021	2.8870	1.2×10^{-3}	147.8	150.9	2.1	33.6	31.2
1208	3.4160	1.4×10^{-3}	175.0	173.7	2.1	24.6	24.4
1390	3.9310	1.6×10^{-3}	201.6	201.9	2.1	21.7	19.4

Supplementary Movie 1 | Transport of one-day-old *Artemia* nauplii at moderate flow velocities in the separation channel. The average flow velocities in the channel are $\bar{u} = 2.6$, 7.3 and $11.9\,\mathrm{mm\,s^{-1}}$. The effect of fluid velocity on the geotaxis of *Artemia* is observed. **a**, Isothermal case, with quantitative data shown by the blue filled upward-pointing triangles in Fig. 3c. **b**, With a temperature differential of 30 K; see the orange hollow upward-pointing triangles in Fig. 3c, which represent the *SR* values. The observations recorded in the videos confirm concurrent phenomena affecting the separation ratio presented in the results of Fig. 3c.

Supplementary Movie 2 | Visualisation of flow patterns and species transport within the laser sheet for single-component saline mixtures. a, Transport of $50\,\mu\mathrm{m}$ tracer particles with a nominal density of $995\,\mathrm{kg\,m^{-3}}$ in deionised (DI) water at $\bar{u} = 2.6\,\mathrm{mm\,s^{-1}}$. The videos show recirculation zones induced by the narrow inlet pipe and honeycomb diffuser near the inlet. These videos were used for PIV analysis shown in Supplementary Fig. 4b. **b**, Transport of one-day-old *Artemia* nauplii at $\bar{u} = 2.6\,\mathrm{mm\,s^{-1}}$ under a non-isothermal flow with a temperature differential of $\Delta T_{\mathrm{wall}} = 30\,\mathrm{K}$. The raw video is shown alongside the corresponding image-processed video, illustrating the spatial distribution of *Artemia* nauplii over the streamwise distances of $x = 370\,\mathrm{mm}$ to $440\,\mathrm{mm}$ from the inlet (see Fig. 5b for quantitative data). The video shows the detection of bubbles caused by surfactant and dissolved air (red circles), *Artemia* tracking (green rectangles), and counting (blue triangles). Distinguishing *Artemia* from bubbles was challenging due to their similar size ranges and colour. **c**, Image-processed isothermal transport of light microplastics (LP) at $\bar{u} = 35.3\,\mathrm{mm\,s^{-1}}$ at streamwise distances of $x = 190\,\mathrm{mm}$ to $260\,\mathrm{mm}$ from the inlet (see Fig. 5c, g for the related data). Some LPs move in the bottom regions, probably due to variations in particle density within and beyond the nominal density range of $985\,\mathrm{kg\,m^{-3}}$ to $1005\,\mathrm{kg\,m^{-3}}$ reported by the supplier (more details in the Methods section). **d** Image-processed isothermal transport of heavy microplastics at $\bar{u} = 82.9\,\mathrm{mm\,s^{-1}}$ over the streamwise region $x = 280\,\mathrm{mm}$ to $350\,\mathrm{mm}$ (corresponding results are shown in Fig. 5e, h).

Supplementary Movie 3 | Thermotactic migration of one-day-old *Artemia* nauplii under a subtle flow and moderate temperature differentials. The transport of *Artemia* nauplii for $\bar{u} = 2.6\,\mathrm{mm\,s^{-1}}$, which is comparable to their swimming speed, is shown under non-isothermal flows with temperature differentials of $\Delta T_{\mathrm{wall}} = 10\,\mathrm{K}$ and 15 K. Based on weighing the top and bottom collected samples following the procedure shown in Fig. 3b, *SR* was determined to be 40.3% and 47.4% for $\Delta T_{\mathrm{wall}} = 10\,\mathrm{K}$ and $\Delta T_{\mathrm{wall}} = 15\,\mathrm{K}$, respectively.

Supplementary Method 1: Hydrodynamics of microplastic transport

1.1 Strength of microplastic–saline coupling

The extent to which microplastics respond to, and are transported by, the bulk fluid flow can be characterised by the particle Stokes number [1] defined as

$$\mathrm{St} = \frac{\tau_\mathrm{p} U}{L}, \tag{1}$$

where U and L are the characteristic velocity and length scale of the flow, respectively, and τ_p is the particle relaxation time defined as

$$\tau_p = \frac{\rho_\mathrm{p} d_\mathrm{p}^2}{18\mu}. \tag{2}$$

Here, ρ_p is the particle density, d_p is the particle diameter and μ is the dynamic viscosity of the fluid. The Stokes number St represents the ratio of the particle response timescale to the characteristic timescale of the flow, and therefore provides a measure of particle–flow coupling. For $\mathrm{St} \ll 1$, MPs respond rapidly to changes in flow and remain closely coupled to the movement of the bulk fluid. As St increases, particle inertia becomes increasingly important, resulting in greater velocity slip and departure from the local fluid trajectory. At $\mathrm{St} \gg 1$, particle inertia dominates over the characteristic flow timescale, leading to weak coupling between the MPs and the surrounding fluid. In the inlet pipe, the higher average flow velocity results in larger St than in the separation channel. Supplementary Fig. 10e shows the CAD model of the separation channel, including the inlet pipe. Supplementary Table 3 lists St values in the inlet pipe and the separation channel for the different experimental flow rates, without accounting for the effects of the honeycomb diffuser or the flow splitter.

1.2 Hydrodynamic entrance length

The hydrodynamic entrance length, L_e, is the streamwise distance required for the velocity profile to develop from its inlet condition to a fully developed state. For an internal flow, L_e depends primarily on the Reynolds number and channel geometry. For a laminar flow in a rectangular duct, it is commonly approximated as [2]

$$L_e \approx 0.05\,\mathrm{Re}\,D, \tag{3}$$

where Re is the Reynolds number and D is the hydraulic diameter. The hydraulic entrance length values for different ranges of flow rate used in the experiments are listed in Supplementary Table 3.

1.3 Velocity profile in the rectangular duct

For a fully developed laminar flow in a rectangular duct shown in Supplementary Fig. 10e, the streamwise velocity distribution is given by [3]

$$u(z,y) = -\frac{6\bar{u}}{a^2 M}\left[y^2 - ay + \frac{8a^2}{\pi^3}\sum_{k=0}^{\infty}\frac{\cosh\left(\frac{(2k+1)\pi z}{a}\right)\sin\left(\frac{(2k+1)\pi y}{a}\right)}{(2k+1)^3\cosh\left(\frac{(2k+1)\pi}{2\alpha}\right)}\right], \tag{4}$$

where $\bar{u}$ is the cross-sectional mean velocity, a and b are the duct dimensions, as shown in Supplementary Fig. 10a, and $\alpha = b/a$ is the aspect ratio. The normalisation factor M is

$$M = 1 - \frac{192\alpha}{\pi^5} \sum_{k=0}^{\infty} \frac{\tanh\left(\frac{(2k+1)\pi}{2\alpha}\right)}{(2k+1)^5}. \tag{5}$$

The corresponding local shear rate in the y direction is

$$\frac{\partial u}{\partial y} = \frac{6\bar{u}}{a^2 M}\left[2y - a + \frac{8a}{\pi^2}\sum_{k=0}^{\infty}\frac{\cosh\left(\frac{(2k+1)\pi z}{a}\right)\cos\left(\frac{(2k+1)\pi y}{a}\right)}{(2k+1)^2\cosh\left(\frac{(2k+1)\pi}{2\alpha}\right)}\right]. \tag{6}$$

For a spherical particle of diameter d_p in contact with the wall, its centre is located at $z = 0$ and $y = d_\mathrm{p}/2$. Substitution into the velocity profile gives

$$u\left(z = 0, y = \frac{d}{2}\right) = 0.1546\bar{u}. \tag{7}$$

Thus, a particle in contact with the wall experiences a local fluid velocity of only approximately 15% of the cross-sectional mean velocity. This reduction in the local carrier-stage velocity is subsequently accounted for in the particle-transport analysis.

1.4 Settling and near-wall transport: A two-trajectory particle model

The transport of an MP particle released from the upper wall and transported downstream is represented by a two-trajectory model shown in Supplementary Fig. 10b between red markers. The first trajectory, between the first and second red marker, corresponds to the settling process of the particle as it is advected across the channel under the combined effects of gravity, buoyancy, hydrodynamic drag and shear-induced lift. The second trajectory, between the second and third red marker, corresponds to that of the near-wall transport after the particle has reached the vicinity of the lower wall. Here, the particle is assumed to remain at an approximately constant wall-normal position and to travel downstream until reaching the channel exit at $x = L$.

Trajectory 1 — Settling

During the settling stage, the particle motion is described by the coupled equations of motion in the streamwise (x) and wall-normal (y) directions,

$$m_\mathrm{p}\frac{\mathrm{d}v_{\mathrm{p},x}}{\mathrm{d}t} = F_{\mathrm{D},x} + F_{\mathrm{L},x}, \tag{8}$$

$$m_\mathrm{p}\frac{\mathrm{d}v_{\mathrm{p},y}}{\mathrm{d}t} = F_{\mathrm{D},y} - (W - F_\mathrm{B}) + F_{\mathrm{L},y}, \tag{9}$$

where $m_\mathrm{p} = \rho_\mathrm{p}\mathcal{V}_\mathrm{p}$ is the particle mass, $\mathcal{V}_\mathrm{p} = \frac{\pi d_\mathrm{p}^3}{6}$ is the particle volume, and ρ_p is the particle density, respectively. Refer to the free-body diagram shown in Fig. 1f(II) for the nomenclature of the forces acting on a particle in the bulk fluid region, away from the wall. Because gravity acts only in the wall-normal direction, it does not directly contribute to the streamwise momentum balance. The buoyancy body force is expressed through $(\rho_\mathrm{p} - \rho_\mathrm{f})\mathcal{V}_\mathrm{p} g_\mathrm{y}$, where ρ_f is the density of the saline solution.

Drag force — Schiller–Naumann correlation. The hydrodynamic drag is calculated using the Schiller–Naumann correlation [4] for the drag coefficient $C_\mathrm{D}$and particle Reynolds number Re_p:

$$C_\mathrm{D} = \frac{24}{\mathrm{Re}_\mathrm{p}}\left(1 + 0.15\,\mathrm{Re}_\mathrm{p}^{0.687}\right), \qquad \mathrm{Re}_\mathrm{p} = \frac{\rho_\mathrm{f} d_\mathrm{p}\,|\mathbf{u} - \mathbf{v}_\mathrm{p}|}{\mu}, \tag{10}$$

$$\mathbf{F}_{\mathrm{D}} = \frac{1}{2} C_{\mathrm{D}} \rho_{\mathrm{f}} A_{\mathrm{p}} \left| \mathbf{u} - \mathbf{v}_{\mathrm{p}} \right| \left(\mathbf{u} - \mathbf{v}_{\mathrm{p}} \right), \tag{11}$$

where $A_{\mathrm{p}} = \pi d_{\mathrm{p}}^2/4$ is the projected particle area, $\mathbf{v}$ is the undisturbed local saline velocity at the particle centre, $\mathbf{v}_{\mathrm{p}}$ is the particle velocity, and μ is the dynamic viscosity of the saline. The Schiller–Naumann correlation accounts for finite particle Reynolds-number effects and is commonly applied to spherical particles for $\mathrm{Re}_{\mathrm{p}} \lessapprox 1000$ [4].

Gravity/buoyancy force. The net body force acting on the MP is

$$\mathbf{W} + \mathbf{F}_{\mathrm{b}} = \frac{\pi}{6} d_{\mathrm{p}}^3 \left(\rho_{\mathrm{p}} - \rho_{\mathrm{f}} \right) \mathbf{g}, \tag{12}$$

where $\mathbf{g}$ is the acceleration of gravity. This formulation simultaneously accounts for gravitational settling and buoyant migration. For $\rho_{\mathrm{p}} > \rho_{\mathrm{f}}$, the particle experiences a net downward force, whereas for $\rho_{\mathrm{p}} < \rho_{\mathrm{f}}$, the force is directed upward. In the present formulation, the gravitational acceleration is aligned with the y direction, i.e., $g_y = 9.8\,\mathrm{m\,s^{-2}}$, $g_x = g_z = 0$.

Saffman lift force. The transverse lift generated by the interaction between particle motion and the local shear flow is described using the Saffman lift formulation [5]

$$F_{\mathrm{L}} = 1.615\, \mu d_{\mathrm{p}}^2 \left(\mathbf{u} - \mathbf{v}_{\mathrm{p}} \right) \left(\frac{|\dot{\gamma}|}{\nu} \right)^{1/2}, \tag{13}$$

where $\nu = \mu/\rho_{\mathrm{f}}$ is the saline kinematic viscosity and $\dot{\gamma} = \frac{\mathrm{d}u}{\mathrm{d}y}$ is the local shear rate. For the predominantly streamwise flow considered here, the Saffman lift acts primarily in the wall-normal direction, and hence $F_{\mathrm{L},y}$ provides the principal lift contribution to the settling trajectory. The original Saffman formulation assumes a small spherical particle in a slowly varying shear flow and is therefore applicable when the particle and shear Reynolds numbers remain sufficiently small [5].
The coupled equations in Trajectory 1 are integrated from the particle's initial position until it reaches a prescribed near-wall position, just $d_{\mathrm{p}}/2 + \delta$ from the wall and assuming $d_{\mathrm{p}} \gg \delta$. For HP and LP particles, the initial position is the upper and lower wall, respectively (Supplementary Fig. 10b). This integration yields both the settling time and the streamwise displacement accumulated during the cross-channel migration. The local saline velocity used in the drag term is evaluated from the fully developed rectangular-duct velocity profile described in Supplementary Method 1.3.

Trajectory 2 — Sliding Once the MP reaches a small separation from the lower wall, its wall-normal motion is assumed to approach a quasi-steady state. The particle is therefore modelled as translating downstream at an approximately constant wall-normal position rather than continuing to change its vertical location. Let δ denote the minimum MP surface-to-wall gap and $a = d_{\mathrm{p}}/2$ the particle radius. The minimum gap between a particle and wall assumed to be equal to the roughness of the particle [6] (the plate roughness was neglected). From the scanning electron microscope (SEM) images of the polyethylene spherical particles used in our experiments that are shown in Supplementary Fig. 10c, the surface roughness is approximately $0.93\,\mu\mathrm{m}$. The distance between the wall and the particle centre is consequently $a + \delta$, a is particle radius, and the dimensionless separation is defined as

$$\epsilon = \frac{\delta}{a}. \tag{14}$$

For a single particle moving near the wall, the forces acting on the particle are depicted in the free-body diagram of Fig. 1f(III). At this stage, the wall-normal force balance is assumed to be quasi-steady,

$$F_{\mathrm{D},y} + F_{\mathrm{L},y} + (\rho_{\mathrm{p}} - \rho_{\mathrm{f}}) V_{\mathrm{p}} g_y = 0, \tag{15}$$

so that the wall-normal acceleration and velocity are negligible. The equilibrium position therefore results from the balance among hydrodynamic drag, shear-induced lift and the net gravitational or buoyant force. Wall-induced modifications to particle lift become

increasingly important as the particle approaches a solid boundary and are therefore accounted for separately from the unbounded-flow settling trajectory [7].

Near-wall tangential drag — Goldman–Cox–Brenner correction. The hydrodynamic resistance opposing particle translation parallel to a wall increases substantially as the particle approaches the boundary. For a sphere translating parallel to a plane wall in the low-Reynolds-number limit, the stream-wise drag can be written as [8]

$$F_{\mathrm{D},x} = -6\pi\mu a\, \lambda_{\parallel}(\epsilon)\, (v_{\mathrm{p},x} - u)\,, \tag{16}$$

where $\lambda_{\parallel}$ is the dimensionless wall-resistance factor and u is the local streamwise saline velocity evaluated at the particle centre. In the near-contact limit, $\epsilon \ll 1$, the resistance factor is approximated by [8]

$$\lambda_{\parallel}(\epsilon) \approx \frac{8}{15} \ln\left(\frac{1}{\epsilon}\right) + 0.9588, \qquad \epsilon = \frac{\delta}{a}. \tag{17}$$

The logarithmic increase in $\lambda_{\parallel}$ reflects the enhanced viscous resistance associated with the thin fluid layer between the particle and the wall [8]. The particle streamwise velocity is therefore determined from the local carrier-stage velocity and the wall-corrected hydrodynamic resistance. The resulting trajectory is integrated downstream until the particle reaches the channel exit at $x = L$.

This two-trajectory model separates the initial cross-channel settling from the subsequent near-wall transport while retaining the principal hydrodynamic mechanisms governing MP motion: particle inertia, drag, gravitational and buoyant forcing, shear-induced lift and wall-modified hydrodynamic resistance. In our analytical method, for each flow rate investigated experimentally, the ordinary differential equations (ODEs) governing particle momentum were numerically solved for light MPs (or LP, with density of $\rho_{\mathrm{LP}} = 995\,\mathrm{kg\,m^{-3}}$) and heavy MPs (or HP, $\rho_{\mathrm{HP}} = 1090\,\mathrm{kg\,m^{-3}}$). The obtained settling distance, settling time and particle exiting time are listed in Supplementary Tables 4 and 5 for LP and HP, respectively. It should be noted that the single-particle analytical model neglects the effects of the inlet pipe, honeycomb diffuser, and flow splitter (Supplementary Fig. 10e). Accordingly, the LP particle was released from a height of $d_{\mathrm{p}}/2$, whereas the HP particle was released from $b - d_{\mathrm{p}}/2$.
To validate the single-particle transport model, its predictions were compared with high-fidelity CFD simulation results obtained using the discrete phase model (DPM) in Ansys Fluent (ver. 2021 R2), a commercial CFD software. The CFD results for LP and HP are presented in Supplementary Tables 4 and 5, respectively. Supplementary Fig. 12 compares the particle trajectory, streamwise velocity, and vertical velocity as functions of time predicted by the analytical single-particle transport model (two-trajectory model) and the CFD simulations. The results are shown for a single LP released from the lower middle of the channel inlet at $\bar{u} = 35.3\,\mathrm{mm\,s^{-1}}$ and a single HP released from the upper middle of the channel inlet at $\bar{u} = 82.9\,\mathrm{mm\,s^{-1}}$.

1.5 Maximum preferable inlet velocity

For a particle to be removed from suspension within the channel without sliding, its residence time along the channel length L must not exceed the time required for it to settle (or rise) to the near-wall region, travelling the channel height b. The schematics of the transport of LP and HP at the maximum preferable velocity are shown in Supplementary Fig. 10d. Following the classical critical-trajectory sedimentation criterion (Hazen [9]), the maximum permissible inlet velocity is defined as the velocity below which particle exit without sliding is guaranteed. The residence time for a particle travelling L at the characteristic streamwise velocity $\bar{u}$ is

$$t_{\mathrm{res}} = \frac{L}{\bar{u}}. \tag{18}$$

The settling time for a particle to traverse the transverse distance $b - d_{\mathrm{p}}$ at its settling terminal velocity v_{s} is

$$t_{\mathrm{s}} = \frac{b - d_{\mathrm{p}}}{v_{\mathrm{s}}}. \tag{19}$$

Setting $t_{\mathrm{res}} = t_{\mathrm{s}}$ defines the limiting maximum operable velocity $\bar{u}_{\max}$, above which particles exit the channel before completing their allowable transverse migration:

$$\bar{u}_{\max} = v_{\mathrm{s}} \frac{L}{b - d_{\mathrm{p}}}. \tag{20}$$

The terminal settling velocity is given by Stokes' law:

$$v_{\mathrm{s}} = \frac{|\rho_{\mathrm{p}} - \rho_{\mathrm{f}}|\, g d_{\mathrm{p}}^2}{18\mu}, \tag{21}$$

where d_{p} and H denote the particle diameter and channel height, respectively, ρ_{p} and ρ_{f} are the particle and fluid densities, μ is the fluid dynamic viscosity, and g is the gravitational acceleration.
The final design equation is therefore:

$$\bar{u}_{\max} = \frac{|\rho_{\mathrm{p}} - \rho_{\mathrm{f}}|\, g d_{\mathrm{p}}^2}{18\mu} \frac{L}{b - d_{\mathrm{p}}}. \tag{22}$$

The corresponding maximum allowable volumetric flow rate is

$$Q_{\max} = \bar{u}_{\max} W b, \tag{23}$$

where W is the width of the separation channel. Since the experimental flow rates ($38\,\mathrm{mL\,min^{-1}}$ to $1390\,\mathrm{mL\,min^{-1}}$) remain below the predicted maximum allowable flow rates for HP ($Q_{\max} \approx 4351\,\mathrm{mL\,min^{-1}}$) and LP ($\approx 1818\,\mathrm{mL\,min^{-1}}$), both particle types are expected to complete the transverse migration (channel height b) to the near-wall region before exiting the channel for all tested operating conditions. Equation 21 uses the unbounded Stokes settling velocity, which neglects the wall corrected drag acting over the last particle diameter of the transverse migration. The resulting $\bar{u}_{\max}$ is therefore an upper bound on the limiting velocity.

Supplementary References

1. Gualtieri, P., Battista, F., Salvadore, F. & Casciola, C. Effect of Stokes number and particle-to-fluid density ratio on turbulence modification in channel flows. *Journal of Fluid Mechanics* **974,** A26. DOI: 10.1017/jfm.2023.851 (2023).
2. Ferreira, G., Sucena, A., Ferrás, L. L., Pinho, F. T. & Afonso, A. M. Hydrodynamic entrance length for laminar flow in microchannels with rectangular cross section. *Fluids* **6,** 240. DOI: 10.3390/fluids6070240 (2021).
3. Xing, D., Yan, C., Wang, C. & Sun, L. A theoretical analysis about the effect of aspect ratio on single-phase laminar flow in rectangular ducts. *Progress in Nuclear Energy* **65,** 1–7. DOI: 10.1016/j.pnucene.2013.01.003 (2013).
4. Schiller, V. L. Uber die grundlegenden Berechnungen bei der Schwerkraftaufbereitung. *Z. Vereines Deutscher Inge.* **77,** 318–321 (1933).
5. Saffman, P. G. The lift on a small sphere in a slow shear flow. *Journal of Fluid Mechanics* **22,** 385–400. DOI: 10.1017/S0022112065000824 (1965).
6. Smart, J. R. & Leighton Jr, D. T. Measurement of the hydrodynamic surface roughness of noncolloidal spheres. *Physics of Fluids A: Fluid Dynamics* **1,** 52–60. DOI: 10.1063/1.857523 (1989).
7. Cherukat, P. & McLaughlin, J. The inertial lift on a rigid sphere in a linear shearflow field near a flat wall. *Journal of Fluid Mechanics* **285,** 407–407. DOI: 10.1017/S0022112094004015 (1995).
8. Goldman, A. J., Cox, R. G. & Brenner, H. Slow viscous motion of a sphere parallel to a plane wall—I Motion through a quiescent fluid. *Chemical Engineering Science* **22,** 637–651. DOI: 10.1016/0009-2509(67)80047-2 (1967).
9. Hazen, A. On sedimentation. *Transactions of the American Society of Civil Engineers* **53,** 45–71. DOI: 10.1061/TACEAT.0001655 (1904).